COMMUNICATIONS IN SCIENCE AND TECHNOLOGY
Homepage: cst.kipmi.or.id

Dense porous monolithic carbon from Indonesian daikon leaf waste via NaOH–CO_2 physicochemical activation for binder-free volumetric supercapacitors

Apriwandi[a,*], Widya Sinta Mustika[b], Julnaidi[c], Della Puspita[a], Rika Taslim[d], Erman Taer[a]

[a]*Department of Physics, University of Riau, 28293 Indonesia*
[b]*Department of Machine Maintenance and Repair, Politeknik Kampar, Riau 28412 Indonesia*
[c]*Department of Mechanical Engineering, Sekolah Tinggi Teknologi Pekanbaru, Pekanbaru 28291 Indonesia*
[d]*Department of Industrial Engineering, Universitas Islam Negeri Sultan Syarif Kasim, Riau 28293 Indonesia*

Article history:
Received: 18 May 2026 / Received in revised form: 15 June 2026 / Accepted: 18 June 2026

Abstract

High-performance volumetric supercapacitors are often limited by the trade-off between porosity and electrode density in biomass-derived carbon. Herein, binder-free monolithic carbon electrodes were produced from Indonesian daikon leaf waste through 0.5 M NaOH pretreatment followed by integrated N_2–CO_2 thermal processing. NaOH activation increased the surface area from 236 to 570 $m^2\ g^{-1}$, increasing carbon purity from 88.34 to 95.45 wt% while retaining 4–5 wt% oxygen functionalities. The activated monolithic carbon electrode (VSAC) delivered a volumetric capacitance of 169 F cm^{-3} at 1 mV s^{-1} and 185 F cm^{-3} at 10 mA cm^{-2} in a symmetric two-electrode configuration without binders or conductive additives. VSAC also retained 83.2% capacitance at high scan rates and achieved 16.01 Wh L^{-1} at 838 W L^{-1}. The improved performance arises from interconnected ion pathways, preserved electrode density, and surface oxygen functionalities, demonstrating a sustainable strategy for practical volumetric supercapacitors.

Keywords: Monolith; volumetric; carbon; electrode; supercapacitor

1. Introduction

The development of advanced electrochemical energy storage devices has become increasingly important in response to the growing demand for clean energy technologies and sustainable resource utilization. Carbon-based supercapacitors have emerged as one of the most promising systems owing to their high cycling stability and rapid charge–discharge capability [1,2]. In recent years, biomass-derived carbon materials have been extensively explored as environmentally benign and cost-effective alternatives to conventional fossil-based synthetic carbons [3,4]. Various biomass sources have been reported as carbon precursors for supercapacitor applications, including bamboo sheath [5], soybean waste [6], hemp core [7], cow urine [8], and palmyra palm tree [9]. These materials generally exhibit high gravimetric capacitance ranging from 229 to 762 F g^{-1}, accompanied by remarkable energy densities approaching 105.8 Wh kg^{-1}, which are competitive with lithium-ion batteries. Nevertheless, most of these studies remain focused on gravimetric performance. Such an approach becomes less representative under practical operating conditions because the electrochemical behavior of highly porous carbon is strongly dependent on low-density architectures. In addition, the majority of reported electrodes are fabricated in powder form using polymeric binders, conductive additives, and external current collectors [10,11]. Consequently, volumetric performance has recently gained increasing attention as a more relevant parameter for next-generation supercapacitor systems [12,13]. In this regard, electrode density becomes a critical factor in achieving high-performance energy storage devices [14,15].

Recent studies have intensively investigated volumetric supercapacitor performance using various material engineering strategies. Zhu et al. (2025) reported biomass-derived basal wood carbon with a volumetric capacitance of 31.4 F cm^{-3} [16]. Meanwhile, Zhang et al. (2025) synthesized CNT/rGO-based electrodes exhibiting a volumetric capacitance of 8.43 F cm^{-3} [17], while similar observations were also reported by Shi et al. (2025) [18]. However, many of these systems still rely on expensive and environmentally unfavorable materials such as graphene and metal oxides. Furthermore, powder-based electrode configurations generally

* Corresponding author.
Email: apriwandi@lecturer.unri.ac.id.
https://doi.org/10.21924/cst.11.1.2026.2000

possess low packing density, which limits the achievable volumetric capacitance. Therefore, the development of binder-free monolithic carbon electrodes has become an important strategy for improving volumetric efficiency while simplifying electrode architecture.

Meanwhile, Indonesia generates approximately 68.7 million tons of waste annually, with organic waste accounting for about (60-65%) of the total composition. This waste primarily originates from household food waste and vegetable residues [19]. Among these vegetable residues, agricultural and kitchen processing byproducts, specifically daikon leaf waste, constitute a notable portion of discarded leafy greens. This condition provides a significant opportunity to convert daikon leaves into high-value functional carbon materials. Daikon leaf waste contains a relatively high lignocellulosic fraction (76%) and possesses a natural biological framework capable of forming porous carbon structures [20]. These characteristics make daikon leaves an attractive biomass precursor for electrochemical energy storage applications [21].

Monolithic carbon electrodes have been reported as binder-free alternatives to conventional powder-based electrodes [22,23]. In contrast, the present study specifically examines how chemical activation regulates the pore–density balance of identically prepared monoliths. VSC and VSAC were fabricated from the same daikon-leaf precursor under identical compaction and N_2–CO_2 thermal-treatment conditions, with 0.5 M NaOH pretreatment as the principal processing difference. NaOH treatment increased the BET surface area from 236 to 570 $m^2\ g^{-1}$ and the total pore volume from 0.1788 to 0.441 $cm^3\ g^{-1}$, while the electrode density decreased moderately from 0.89 to 0.82 g cm^{-3}. This structural modification increased the volumetric capacitance from 78 to 169 F cm^{-3} at 1 mV s^{-1}. Thus, the contribution of this study lies in quantitatively demonstrating the relationship between activation-induced pore development, retained monolith density, and volumetric charge storage, rather than claiming novelty for the monolithic configuration itself.

2. Materials and Methods

2.1. Preparation of biomass precursors

Indonesian vegetable waste, specifically daikon leaf waste sourced from a traditional market in Pekanbaru, Indonesia, served as the primary carbon precursor. The biomass underwent a meticulous cleaning process using deionized water to eliminate contaminants and residual soil particles. Following this, the material was cut into smaller pieces and effectively dried under direct sunlight until there were no further changes in mass. The dried biomass was then transformed into a fine powder through a mechanical ball-milling process, followed by sieving with a 200-mesh filter to ensure a uniform particle size distribution. Our synthesis procedures were strategically designed to embrace a low-chemical-consumption approach, significantly reducing secondary waste generation during carbon production. Sodium hydroxide (NaOH), purity 98%, supplied from Sigma-Aldrich, supplier: CV Pulo Batu Pekanbaru, Indonesia, acted as the activating reagent, while a sulfuric acid solution was utilized as the electrolyte in the electrochemical testing phase.

2.2. Synthesis of monolithic carbon electrodes

To induce pore formation and preserve the monolithic architecture, the biomass powder was initially immersed in a dilute NaOH solution (0.5 M) using a precursor-to-solution ratio of 1:5. The suspension was continuously stirred at 300 rpm and maintained at 80°C for 2.5 h to promote homogeneous penetration of the activating species into the biomass matrix. After impregnation, the slurry was dried to obtain a free-flowing powder. Approximately 0.70 g of the dried biomass powder was placed into a cylindrical stainless-steel die with an internal diameter of 20 mm. The powder was compacted using a hydraulic press at an applied load 8 metric ton and it became a pellet form. No polymeric binder or conductive additive was introduced during compaction. The resulting green pellets had an average diameter of approximately 20 mm and a thickness of 2 mm before thermal treatment. The compacted pellets were subsequently subjected to a one-step integrated pyrolysis (carbonization and physical activation) process at 850°C under a controlled dual-gas environment consisting of N_2 and CO_2. The gas atmosphere was carefully regulated throughout the heating, activation, and cooling stages to simultaneously promote carbonization, pore evolution, and stabilization of naturally derived oxygen functionalities. During thermal treatment, significant dimensional shrinkage occurred, leading to the formation of dense monolithic carbon structures with interconnected porosity. The resulting products were repeatedly washed using deionized water for several days until neutral pH was achieved in order to remove residual inorganic species and excess activating agent. The activated monolithic carbon was denoted as VSAC, whereas the sample synthesized without NaOH treatment was labeled VSC.

2.3. Structural and morphological characterization

The dimensional changes and density variations before and after pyrolysis were assessed to investigate the structural evolution of monolithic carbon during thermochemical treatment. The crystalline properties were analyzed using X-ray diffraction (XRD) with a Shimadzu MAXima_7000, which operated with Cu Kα radiation (λ = 1.560 Å) at 40 kV and 40 mA. Structural parameters, including interlayer spacing and crystallite dimensions, were estimated using the Bragg and Debye–Scherrer methods. Surface morphology and pore development were examined through scanning electron microscopy (SEM) using a JEOL JSM-IT200. The elemental composition and residual inorganic species were identified with energy-dispersive X-ray spectroscopy (EDS) analysis, which was conducted at 15 kV. The surface area (S_{BET}) and pore distribution properties studied using a Quantachrome Nova 4200e analyzer (version 11.03) at a temperature of 77.35 K.

2.4. Electrochemical measurements

The electrochemical performance was evaluated using a symmetric two-electrode laboratory cell to provide a device-

level comparison between VSC and VSAC under identical operating conditions. The monolithic carbon pellets were directly used as electrodes without the addition of binder or conductive carbon. To maintain ion transport while preventing direct electrical contact between the electrodes, an eggshell membrane combined with Whatman Grade 1 paper was employed as the separator. The assembled cell was immersed in a 1 M H_2SO_4 electrolyte and operated within a potential window of 0 to 1 V. Electrochemical characterization was conducted using cyclic voltammetry (CV) and galvanostatic charge-discharge (GCD) with Corrtest CS2350 integrated with UR-Rad-Er ver. 2810-2018 instruments. The electrochemical response of the monolithic electrodes was examined under various scan rates and current densities to assess volumetric charge storage behavior, rate capability, and ion transport characteristics. Volumetric capacitance, energy density, and power density were calculated based on Eqs. (1)–(6).

$$C_g = (I \cdot \Delta t)/m \cdot \Delta V \quad (1)$$

$$C_v = C_g \cdot \rho \quad (2)$$

$$E_g = ½.7 \cdot C_g \cdot V^2 \quad (3)$$

$$E_v = E \cdot \rho \quad (4)$$

$$P_g = 3600 \cdot E_g/\Delta t \quad (5)$$

$$P_v = P_g \cdot \rho \quad (6)$$

where (C_g) is the gravimetric capacitance (F g^{-1}), (C_v) is the volumetric capacitance (F cm^{-3}), (I) is the discharge current (A), (Δt) is the discharge time (s), (m) is the active mass of the working electrode (g), (ΔV) is the effective discharge potential window (V), and (ρ) is the working-electrode density (g cm^{-3}). The working electrode density was determined by dividing the dry mass of each monolithic electrode by its geometric volume after thermal treatment. The volume of the cylindrical electrode was calculated as ($V= \pi(d/2)2t$), where (d) and (t) are the measured diameter and thickness, respectively. (E_g) and (E_v) denote the gravimetric energy density (Wh kg^{-1}) and volumetric energy density (Wh L^{-1}), respectively, whereas (P_g) and (P_v) represent the gravimetric power density (W kg^{-1}) and volumetric power density (W L^{-1}), respectively.

3. Results and Discussion

The fundamental evaluation in developing biomass-derived carbon electrodes for supercapacitor applications centers on optimizing volumetric density, as this parameter directly governs the amount of charge stored per unit volume of the device. In contrast to gravimetric performance, which is predominantly dictated by specific surface area, volumetric performance requires a more intricate balance among material density, pore architecture, and electrolyte ion accessibility [24]. Therefore, a detailed assessment of geometric dimensions and bulk density of the solid carbon is essential to elucidate the structural evolution during the physicochemical activation process.

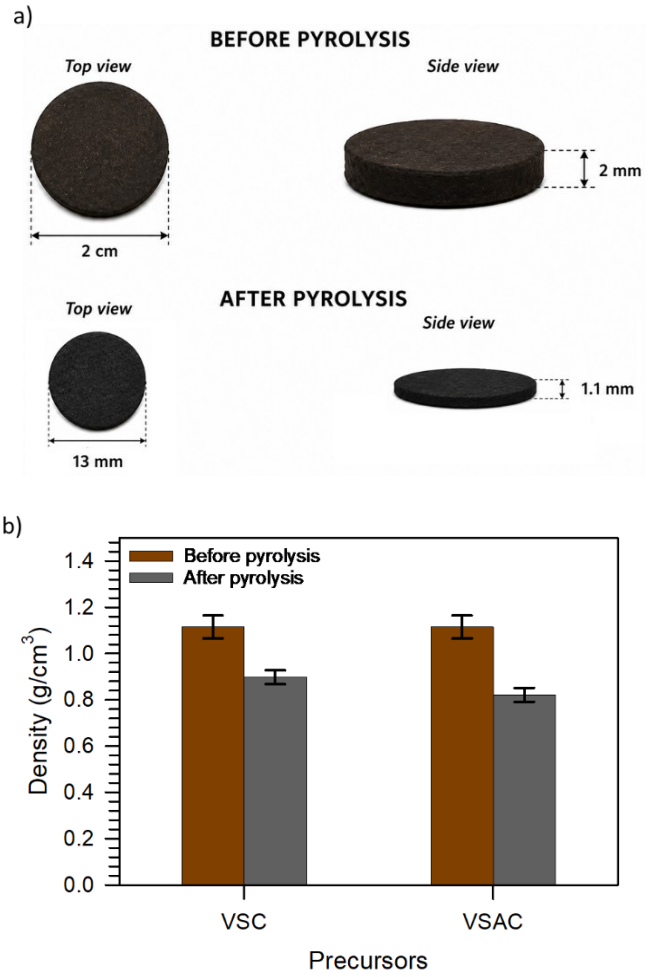

Fig. 1. a) geometric dimensions, and b) density shrinkage of VSC and VSAC precursor

As illustrated in Fig. 1(a), the solid precursor prior to pyrolysis exhibits a relatively homogeneous macroscopic appearance, characterized by a dark brown color and a compact surface texture, suggesting a uniform mass distribution with negligible porosity. The initial dimensions were measured to be approximately 2 cm in diameter and 2 mm in thickness (measurement error ±0.05), representing a dense precursor state. Following carbonization and combined physicochemical activation, pronounced transformations are observed in both visual appearance and dimensional characteristics. The material turns black, indicating an increased degree of carbonization and the formation of conjugated aromatic structures. Concurrently, the diameter and thickness shrink to approximately 13 mm and 1.1 mm (measurement error ±0.05), respectively. This dimensional reduction reflects a structural shrinkage phenomenon driven by volatile release, decomposition of organic constituents, and reorganization of the carbon framework [25–27]. This shrinkage introduces a dual effect. On one hand, volume contraction contributes to enhanced local packing density; on the other hand, pore generation leads to an overall reduction in bulk density, particularly in samples subjected to NaOH activation. As shown in Fig. 1(b), the precursor density decreases from 1.115 g cm^{-3} before pyrolysis to 0.89 g cm^{-3} (without chemical activation) and further to 0.82 g cm^{-3} (with NaOH activation). This reduction indicates that the activation

process not only develops the pore network but also increases the void fraction within the carbon matrix [28,29]. These findings highlight an inherent trade-off between porosity development and material densification. While chemical activation promotes extensive pore formation, which is beneficial for enhancing specific capacitance, it simultaneously compromises volumetric density.

The solid monolithic electrode design employed in this study becomes particularly advantageous. The binder-free carbon solid enables controlled shrinkage to preserve relatively high density, while still maintaining an interconnected pore network that facilitates efficient ion transport throughout the electrode structure [30]. The physical and chemical activation contributions should be distinguished in interpreting these structural changes. Both VSC and VSAC were exposed to the same N_2–CO_2 thermal treatment. During carbonization, the inert N_2 atmosphere facilitated volatile removal and the formation of the carbon framework. At 850°C, CO_2 acted as a physical activating agent through the partial gasification of reactive carbon sites according to ($C + CO_2 \rightarrow 2CO$), thereby opening initially inaccessible voids and promoting pore development [31,32]. The combined effects of carbonization and CO_2 activation were accompanied by a density decrease from 1.115 g cm^{-3} in the initial pellet to 0.89 g cm^{-3} in VSC. The additional NaOH pretreatment applied to VSAC intensified structural etching and inorganic-species removal, resulting in a further density decrease to 0.82 g cm^{-3} and a more open morphology. Because an N_2-only control was not included, the individual contribution of CO_2 activation cannot be quantitatively separated; therefore, the VSC–VSAC comparison specifically represents the additional effect of NaOH pretreatment under identical CO_2 activation conditions.

The microstructural evolution of the solid carbon derived from the synthesis route was systematically examined using XRD, as presented in Fig. 2. In general, both precursors exhibit diffraction patterns characteristic of non-graphitic carbon, marked by two broad diffraction bands commonly regarded as the “fingerprint” of amorphous carbon. The first diffuse peak appears in the range of $2\theta \approx 23–25°$, corresponding to the (002) plane, while the second broad feature is observed at $2\theta \approx 43–45°$, associated with the (100) plane [33,34]. According to the standard graphite reference (JCPDS No. 41-1487), the ideal diffraction positions for crystalline graphite are located at approximately 26.5° for the (002) reflection and 44° for the (100) reflection. The noticeable shift of these peaks toward lower diffraction angles, coupled with their significant broadening, indicates an expanded interlayer spacing and a high degree of structural disorder in both samples. Specifically, the calculated d_{002} values (3.731 Å for VSC and 3.594 Å for VSAC) are substantially larger than that of crystalline graphite (3.354 Å), reflecting interlayer expansion induced by structural defects, residual functional groups, and lattice distortions [35]. This expansion, reaching approximately 7–11%, confirms the formation of a turbostratic carbon structure with poorly aligned graphene layers [36]. Such turbostratic configurations, characterized by small domain sizes and abundant defects, are advantageous for enhancing electrolyte ion accessibility, thereby contributing to improved electrochemical performance, particularly in terms of volumetric capacitance [37]. In addition, the obtained d_{100} values (2.001 Å for VSC and 1.050 Å for VSAC) suggest limited in-plane ordering within the graphitic domains, which is typical for biomass-derived carbons. A notable distinction between VSC and VSAC lies in the peak width and intensity. The VSAC exhibits broader and more diffuse peaks in both reflections, indicating a higher degree of amorphization and fragmentation of crystalline domains induced by NaOH chemical activation [38,39]. This activation process not only promotes pore development but also disrupts small graphitic domains into more dispersed structural units, leading to a reduction in the crystallite height (Lc decreases from 7.785 Å to 5.639 Å). Meanwhile, Lc can be correlated with surface area through empirical relationships reported in previous studies [40,41]. The surface area was further confirmed in N_2 gas adsorption. Interestingly, the lateral crystallite size (La) increases from 15.435 Å in VSC to 21.393 Å in VSAC. This suggests that, despite vertical fragmentation along the c-axis, a relative lateral expansion of graphitic domains occurs, likely due to structural rearrangement and reorganization of carbon fragments during activation. The XRD parameter was detailed in Table 1.

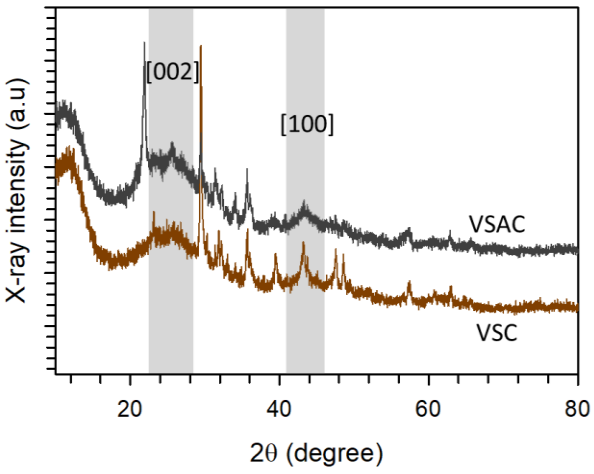

Fig. 2. XRD pattern of VSC and VSAC

Table 1. XRD parameter

Precursor	$2\theta_{002}$ (°)	$2\theta_{001}$ (°)	d_{002} (Å)	d_{100} (Å)	L_c (Å)	L_a (Å)
VSC	23.83	45.13	3.731	2.001	7.785	15.435
VSAC	24.76	44.14	3.594	1.050	5.639	21.393

Beyond the amorphous features, the presence of sharp diffraction peaks in the VSC pattern indicates the existence of minor crystalline phases originating from mineral residues, such as SiO_2, $CaCO_3$ (JCPDS 05-0586), CaO (JCPDS 37-1497), and MgO (JCPDS 45-0946). The sharp peak observed at approximately 22° in the VSAC pattern is tentatively attributed to a trace crystalline silica phase originating from the inherent mineral components of daikon leaves. This assignment is supported by the residual Si content detected by EDS in VSAC. In contrast, the broader feature at higher angles corresponds to the disordered carbon (002) reflection. These peaks appear at their characteristic diffraction angles

and imply that the initial carbonization process does not completely eliminate inorganic components inherent to the biomass precursor [42,43]. In contrast, the VSAC sample shows a significant attenuation of these sharp peaks, demonstrating that chemical activation effectively removes or decomposes these mineral phases, resulting in a purer carbon matrix. This XRD analysis reveals that the combined carbonization and physicochemical activation route not only induces a highly disordered turbostratic carbon structure but also governs the interplay between microstructural disorder and pore development. This structural configuration is critical for achieving enhanced ion transport and optimized volumetric electrochemical performance.

The examination of surface morphology via SEM imaging is crucial to further substantiate the proposed microstructural evolution induced by carbonization and physicochemical activation, as previously discussed based on XRD analysis. SEM images of both precursors are presented in Fig. 3 at a magnification of 5000×, providing sufficient resolution to resolve surface characteristics and pore development at the micrometer scale. As shown in Fig. 3(a), VSC exhibits a relatively dense and compact surface morphology with a predominantly smooth texture and only weak indications of open pore formation. The structure is dominated by tightly bound carbon aggregates, forming continuous domains without significant voids. Several small particles dispersed across the surface can be associated with inorganic residues that were not completely decomposed during the thermochemical process. This observation suggests that the initial carbonization step primarily facilitates the formation of a carbon framework, without substantially developing an interconnected pore network. In contrast, Fig. 3(b) reveals a markedly different morphological profile for the VSAC sample subjected to NaOH chemical activation. The carbon surface appears significantly rougher and more heterogeneous, with clearly defined open pores and perforated features resembling a honeycomb-like framework. These pores exhibit a wide size distribution, ranging from micropores to interconnected mesopores, indicating that the activation process effectively etches the carbon matrix and generates more accessible diffusion pathways [44,45]. In addition, the presence of thinner and more fragmented carbon walls suggests that chemical interactions between carbon and the activating agent induce localized weakening of the carbon framework, which subsequently evolves into a more complex porous architecture [46].

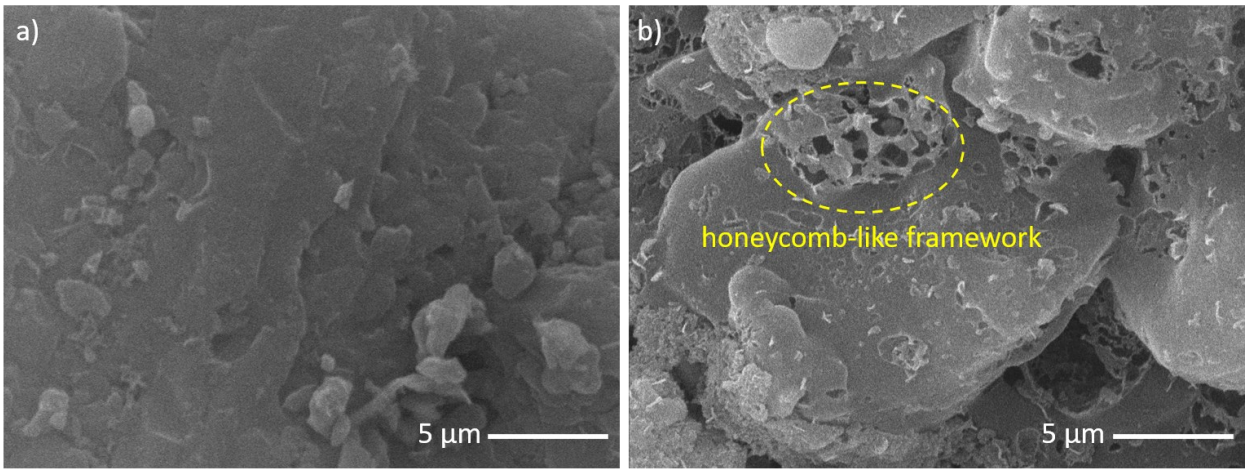

Fig. 3. SEM image for a) VSC, and b) VSAC

This morphological transformation is consistent with the previously discussed density and XRD results, where increased porosity in VSAC correlates with a reduction in bulk density and a higher degree of structural disorder. Importantly, the presence of open pores and an interconnected network is critical for supercapacitor applications, as it enhances electrolyte ion accessibility throughout the electrode volume [47,48]. Beyond providing a larger active surface area, such a structure also facilitates more efficient ion transport, thereby minimizing diffusion resistance at high charge–discharge rates [49]. The SEM observations indicate that the additional NaOH pretreatment, superimposed on the common CO_2 physical activation applied to both samples, promoted a more open and interconnected surface morphology in VSAC than in VSC.

Elemental composition analysis using EDS was conducted to evaluate the carbon purity and to identify residual inorganic elements remaining within the solid carbon matrix. The quantified elemental data summarized in Table 2 reveal a pronounced compositional difference between VSC, which was produced without chemical activation, and VSAC, which underwent chemical activation. This contrast directly reflects the effectiveness of the applied thermochemical treatment. For VSC, the carbon content is measured at 88.34%, accompanied by a relatively high oxygen content of 9.65%.

Table 2. Elemental composition

Precursors	C (% wt)	O (% wt)	Mg (% wt)	Si (% wt)	Cl (% wt)	K (% wt)	Ca (% wt)	Fe (% wt)	Zn (% wt)
VSC	88.3	9.65	0.26	0.61	0.18	0.07	0.49	0.20	0.19
VSAC	95.4	4.01	0.06	0.05	0.15	0.14	0.12	0.04	0.00

The presence of oxygen at this level suggests that oxygen-containing functional groups, such as hydroxyl, carbonyl, or carboxyl species, are not fully eliminated during the carbonization stage [50,51]. In addition, minor elements

including Mg (0.26%), Si (0.61%), Cl (0.18%), K (0.07%), Ca (0.49%), Fe (0.20%), and Zn (0.19%) are detected, which are typically associated with the inherent mineral constituents of the biomass precursor. The persistence of these elements indicates that carbonization alone, without subsequent chemical activation, is insufficient to completely remove inorganic residues. This observation is consistent with the presence of crystalline impurity peaks identified in the XRD analysis. In contrast, VSAC exhibits a substantial increase in carbon purity to 95.45%, along with a marked reduction in oxygen content to 4.01%. This change indicates that NaOH-based chemical activation not only facilitates pore development but also effectively removes oxygen-containing functional groups through deoxygenation and partial gasification reactions [52]. Furthermore, most metallic and mineral elements show a drastic reduction in concentration, with Zn no longer detected. The significant decrease in Mg, Si, Ca, and Fe suggests that chemical activation functions as a leaching mechanism, dissolving or extracting inorganic species from the carbon matrix [53]. Interestingly, the K content in VSAC shows a slight increase compared to VSC, which is likely associated with residual species originating from the alkali activation process. However, its relatively low concentration indicates that the post-activation washing procedure is sufficiently effective in minimizing residual activating agents. The increase in carbon fraction, coupled with the significant reduction of impurity elements, has direct implications for enhanced electrical conductivity and improved electrochemical stability. The higher purity achieved in VSAC therefore represents a critical factor in optimizing the volumetric performance of supercapacitors, particularly by reducing internal resistance and facilitating more efficient charge transport within the solid electrode system.

To quantitatively verify the pore development indicated by the SEM observations, the textural properties of VSC and VSAC were evaluated using N_2 adsorption–desorption analysis, as shown in Fig. 4. Both samples exhibit combined Type I/IV adsorption characteristics, indicating the coexistence of micropores and mesopores. The pronounced N_2 uptake at low relative pressure is associated with micropore filling, whereas the hysteresis observed over the intermediate-to-high relative-pressure region reflects capillary condensation within mesopores. Compared with VSC, VSAC shows substantially higher N_2 uptake throughout the entire relative-pressure range, confirming that NaOH pretreatment markedly increased the accessible pore volume. VSC exhibited a surface area of 236 $m^2\ g^{-1}$, comprising micropore and mesopore surface areas of 206 and 30 $m^2\ g^{-1}$, respectively, with a total pore volume of 0.1788 $cm^3\ g^{-1}$. In comparison, VSAC achieved a surface area of 570 $m^2\ g^{-1}$, including 445 $m^2\ g^{-1}$ of micropore area and 125 $m^2\ g^{-1}$ of mesopore area, together with a total pore volume of 0.441 $cm^3\ g^{-1}$. Thus, NaOH pretreatment increased the surface area and total pore volume by approximately 2.42- and 2.47-fold, respectively. Notably, the mesopore surface area increased more strongly than the micropore area, raising its contribution from 12.7% in VSC to 21.9% in VSAC.

The pore-size distribution in Fig. 4(b) further reveals a dominant pore population close to 1 nm and a broader mesopore distribution at approximately 2–6 nm. These features are considerably more developed in VSAC, demonstrating the formation of a hierarchical micro–mesoporous structure. The micropores provide abundant ion-adsorption sites, while the mesopores can facilitate electrolyte penetration and connect the internal pore network. Despite the pronounced increase in surface area and pore volume, the electrode density decreased only from 0.89 to 0.82 g cm^{-3}. This result demonstrates that NaOH-assisted activation effectively improved pore accessibility while retaining a relatively dense monolithic framework, providing a favorable balance between porosity and volumetric charge-storage capability.

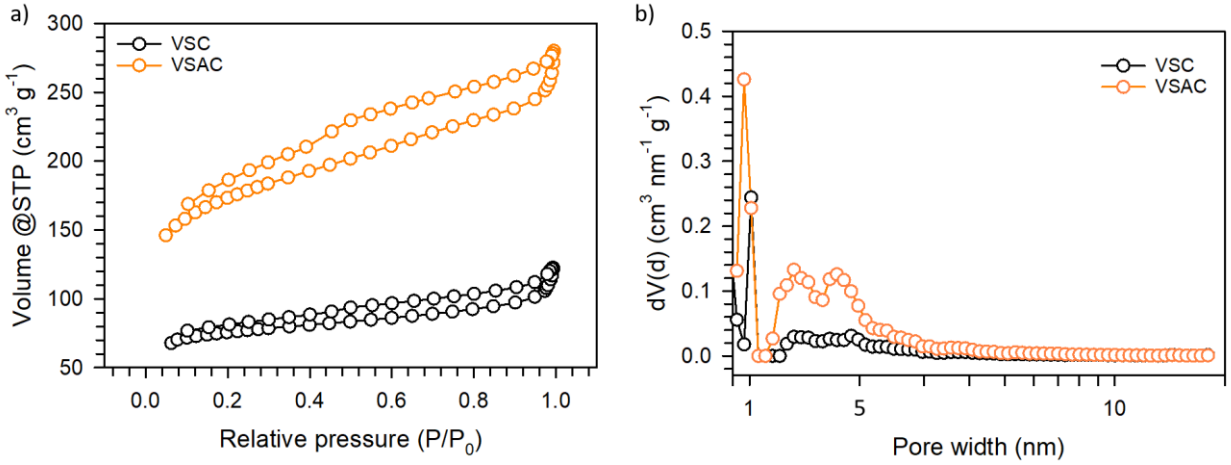

Fig. 4. (a) N_2 adsorption–desorption isotherms and (b) pore-size distributions of VSC and VSAC

The electrochemical performance of VSC and VSAC electrodes was evaluated using a symmetric two-electrode configuration to represent realistic supercapacitor operating conditions. In this system, the carbon electrodes were designed as solid monolithic structures without binders or conductive additives, allowing the obtained electrochemical response to directly reflect the intrinsic characteristics of the synthesized carbon materials. The charge-storage behavior was initially investigated through cyclic voltammetry, as presented in Fig. 5. In general, both electrodes exhibit quasi-

rectangular CV profiles within the potential window of 0–1 V, indicating that the charge-storage mechanism is predominantly governed by electric double-layer (EDL) capacitance [54]. Nevertheless, the CV profiles of VSC and VSAC display notable differences, suggesting that pore development and carbon microstructural configuration strongly influence electrolyte ion kinetics and volumetric charge-storage efficiency. As shown in Fig. 5(a), VSC exhibits a leaf-like CV profile with a pronounced diagonal tendency.

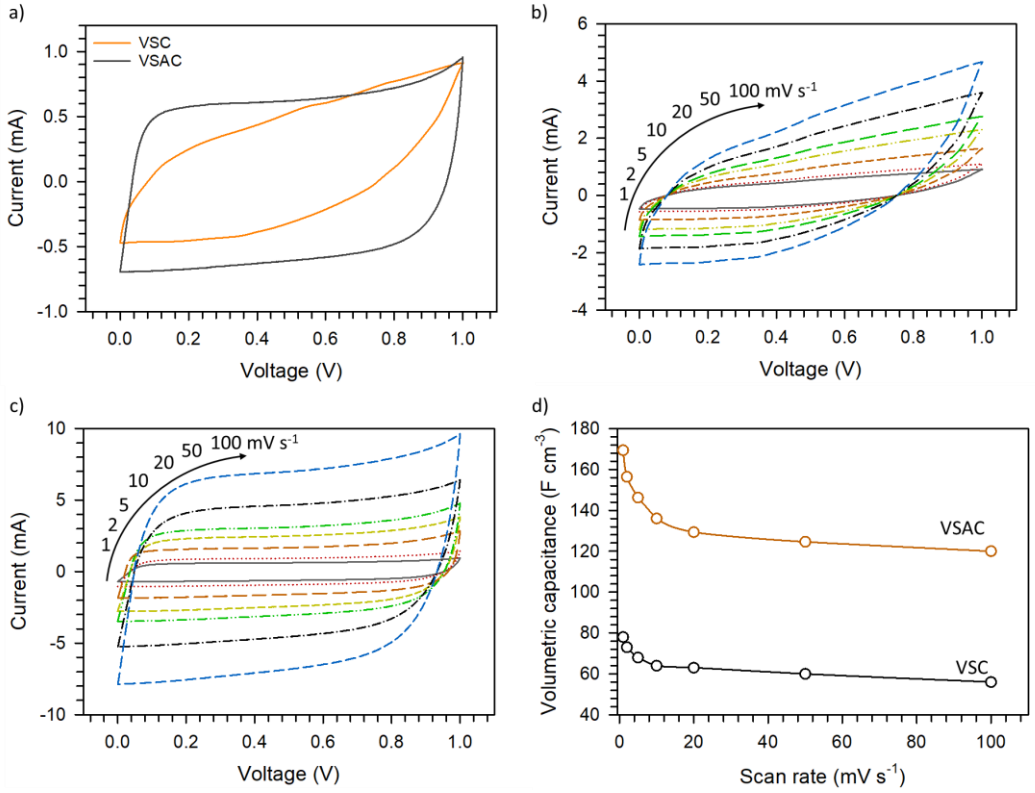

Fig. 5. CV curve of VSC and VSAC in 1mV s^{-1}, (b) CV curve of VSC in 1-100 mV s^{-1}, (c) CV curve of VSAC in 1-100 mV s^{-1}, and (d) Volumetric capacitance vs. scan rate

This characteristic indicates limited electric double-layer formation due to insufficient ion accessibility throughout the electrode volume. The relatively compact carbon structure with poorly developed open pores restricts electrolyte ions from effectively interacting beyond the external surface of the carbon matrix [55]. Consequently, ion diffusion resistance increases, leading to a less homogeneous charge distribution within the electrode volume. As a result, the current response toward potential variation becomes less ideal and the enclosed hysteresis area remains relatively small. This behavior directly contributes to the relatively low volumetric capacitance of 78 F cm^{-3} at 1 mV s^{-1}. In contrast, VSAC exhibits a CV profile much closer to an ideal rectangular shape, accompanied by a broader hysteresis area and a more symmetrical current response. This improvement demonstrates that NaOH chemical activation effectively enhances the capacitive behavior of the electrode through the formation of a more developed and interconnected pore network [56]. The open porous structure facilitates faster electrolyte ion diffusion toward internal active sites, allowing the ion adsorption–desorption process to proceed more reversibly [57]. Furthermore, the turbostratic structure identified from XRD analysis, together with the honeycomb-like morphology observed from SEM imaging, supports the formation of more continuous ion transport pathways within the dense carbon matrix. As a result, the volumetric capacitance of VSAC increases nearly twofold compared to VSC, reaching 169 F cm^{-3} at 1 mV s^{-1}. This substantial enhancement indicates that chemical activation successfully optimizes the balance between pore development and solid-electrode density. This finding is particularly important because increasing porosity in carbon materials is commonly accompanied by a significant reduction in volumetric density. However, the monolithic electrode strategy employed in this work enables the development of an interconnected porous framework without excessively compromising electrode density, thereby preserving high volumetric performance [58,59]. Although both electrodes exhibit predominantly EDL characteristics, the CV profiles are not perfectly rectangular, indicating the presence of limited pseudocapacitive contributions. Slight deviations near the corner regions of the curves are likely associated with residual oxygen-containing functional groups remaining on the carbon surface. These oxygen functionalities may induce shallow faradaic reactions at the electrode–electrolyte interface, providing additional charge-storage contributions [60,61]. However, such contributions do not dominate the overall energy-storage mechanism.

The improved electrochemical performance of VSAC is primarily associated with the combined changes in pore structure and retained electrode density. NaOH pretreatment increased the surface area from 236 to 570 m^2 g^{-1} and the total pore volume from 0.1788 to 0.441 cm^3 g^{-1}. The micropore

area increased from 206 to 445 $m^2\ g^{-1}$, while the mesopore area increased more markedly from 30 to 125 $m^2\ g^{-1}$. These textural changes were accompanied by only a decrease in electrode density from 0.89 to 0.82 g cm^{-3} and an increase in volumetric capacitance from 78 to 169 F cm^{-3} at 1 mV s^{-1}. Therefore, the enhanced performance is reasonably associated with the increased ion-accessible surface and improved micro–mesopore connectivity while retaining a relatively dense monolithic structure [62]. In contrast, the oxygen content decreased from 9.65 wt% in VSC to 4.01 wt% in VSAC. This trend indicates that oxygen content alone cannot explain the higher capacitance of VSAC. Although residual oxygen species may influence electrode wettability, their specific chemical states and individual capacitance contributions cannot be determined from EDS analysis. Accordingly, the revised manuscript does not assign a quantitative or dominant role to oxygen functionalities.

The influence of scan rate on charge-storage kinetics is presented in Fig. 5(b–c). As the scan rate increases from 1 to 100 mV s^{-1}, both electrodes undergo progressive curve deformation toward a more diagonal shape due to diffusion limitations arising from shorter ion response times. Under these conditions, electrolyte ions tend to access only the outer surface regions, leaving part of the internal active sites underutilized. Nevertheless, VSAC maintains its quasi-rectangular profile more effectively than VSC, indicating that its more open and interconnected pore network facilitates more efficient ion transport even under rapid charging conditions. This phenomenon is further confirmed by the rate capability results shown in Fig. 5(d). VSC retains approximately 71.9% of its volumetric capacitance at high scan rates, whereas VSAC exhibits superior retention of 83.2%. The higher retention demonstrates that chemical activation not only increases the number of accessible active sites, but also significantly improves ion transport dynamics within the solid electrode architecture.

The charge storage characteristics of solid electrodes constructed from VSC and VSAC were analyzed using GCDs, which served to evaluate charge transfer stability, electrochemical reversibility, and ion kinetics resistance under constant current conditions. Unlike CV, GCD provides a highly accurate representation of the electrode's true energy storage capabilities during the charge-discharge cycle. The GCD curves for both electrodes are presented in Fig. 6. In Fig. 6(a), both samples display a symmetrical charge-discharge pattern devoid of a clear potential plateau, indicating that the energy storage mechanism is predominantly governed by EDL. The lack of a faradaic plateau confirms that redox reactions on the carbon surface are minimal and do not dominate the charge storage mechanism [63]. Nonetheless, the curves for both electrodes exhibit slight deviations from a linear shape, particularly in the initial charge and discharge stages. This deviation reflects a weak pseudocapacitive contribution attributed to oxygen-based functional groups present on the carbon surface [64]. Groups such as hydroxyl, carbonyl, and carboxyl enhance the wettability of the electrode surface, facilitating rapid ion penetration into the pores. Furthermore, these groups promote shallow faradaic reactions, significantly contributing to charge accumulation [65]. This effect is especially pronounced in the VSAC electrode, where a more open pore distribution allows residual oxygen groups to effectively interact with electrolyte ions.

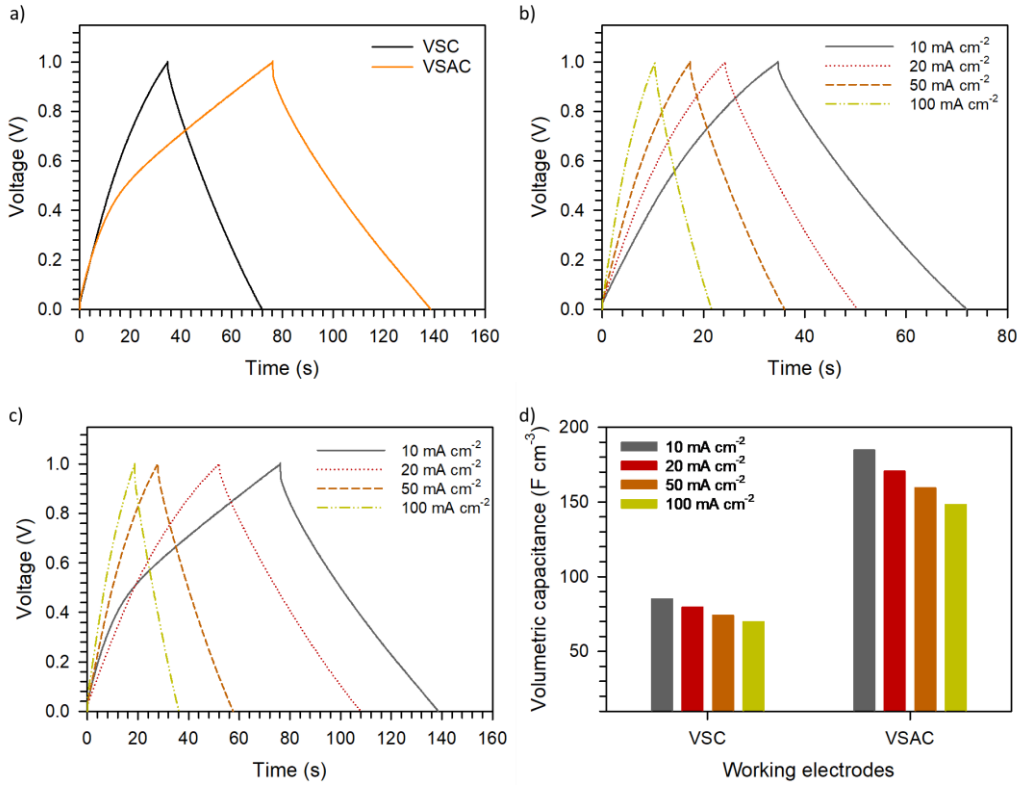

Fig. 6. GCD curve of VSC and VSAC in 10mA cm^{-2}, (b) GCD curve of VSC in 10-100 mA cm^{-2}, (c) GCD curve of VSAC in 1-100mA cm^{-2}, and (d) Volumetric capacitance vs. current density

The differences in curve characteristics between VSC and VSAC underscore the substantial impact of chemical activation on charge storage dynamics. VSC demonstrates a relatively short discharge time with a steeper curve slope, clearly indicating that charge discharge occurs rapidly due to a limited active area accessible to electrolyte ions. The dense carbon structure confines ions to interact predominantly on the external surface, restricting the energy storage capacity within the electrode volume, with a recorded volumetric capacitance of 85 F cm^{-3} at 10 mA cm^{-2}. In sharp contrast, VSAC exhibits an extended discharge time and a remarkably stable charge-discharge profile. This emphatically demonstrates that NaOH activation creates a highly efficient ion diffusion pathway through the interconnected pore network, allowing for more effective ion adsorption-desorption throughout the electrode volume. As a result, the recorded volumetric capacitance ascends to 184 F cm^{-3} at 10 mA cm^{-2}. The GCD curves at varying current densities, illustrated in Fig.s 6(b) and 6(c), reveal that increasing the current density from 10 to 100 mA cm^{-2} significantly shortens the discharge time for both electrodes due to reduced diffusion time for ions to reach internal active sites. However, VSAC maintains a more symmetrical curve shape when compared to VSC, indicating that the activated pore structure successfully supports stable ion kinetics, even under rapid charge conditions. This growth in pore network not only enhances the active surface area but also shortens the ion transport pathway within the solid carbon matrix. Fig. 6(d) decisively demonstrates how both electrodes sustain their volumetric capacitance as current density increases from 10 to 100 mA cm^{-2}. In general, it is evident that increasing current density leads to a decline in capacitance due to the limited time for ions to access all active sites within the electrode. VSC experiences a decrease in capacitance from 85 to 69 F cm^{-3}, yielding a retention rate of approximately 81.2%. This outcome highlights that the relatively compact carbon structure confines electrolyte ions to the outer surface during fast charging, resulting in underutilization of some internal active sites. Conversely, VSAC maintains a significantly higher capacitance, reducing from 185 to 148 F cm^{-3}, with a retention rate of about 84.9%. This outcome confirms that chemical activation successfully created an open and interconnected pore network capable of preserving ion transport efficiency, even at elevated current densities. While both electrodes show relatively similar capacitance retention, VSAC boasts a dramatically larger absolute capacitance across the entire current density range, clearly indicating that the increase in porosity does not lead to a significant loss in electrode density. Table 3 presents a comparison of selected carbon-based supercapacitors under different testing conditions. VSAC delivered 185 F cm^{-3} at 10 mA cm^{-2} with an electrode density of 0.82 g cm^{-3} in 1 M H_2SO_4. Although direct ranking is limited by differences in electrolyte, electrode density, and device configuration, VSAC demonstrates competitive volumetric performance using a binder- and additive-free monolithic electrode.

Table 3. Comparison of reported volumetric capacitance values for selected carbon-based supercapacitors under different testing conditions

Carbon precursor/material	Electrode architecture	Electrolyte	S_{BET} (m^2 g^{-1})	ρ (g cm^{-3})	Testing condition	(C_v) (F cm^{-3})	Ref
B-doped holey graphene/activated carbon (BHG600/AC)	Composite powder electrode with binder; symmetric coin cell	1 M $TEABF_4$	Not report	Not report	0.5 A g^{-1}	52.9	[14]
N/O co-doped activated carbon from glucose and egg solution	Powder-based activated carbon electrode; symmetric two-electrode cell	1 M H_2SO_4	Not report	0.76	0.5 A g^{-1}	276	[15]
Moringa oleifera leaves	Binder-free consolidated carbon disc; symmetric two-electrode cell	1 M H_2SO_4	412.196	0.560	1 A g^{-1}	101.61	[23]
N,O-doped activated carbon derived from expired coffee (HCDC)	Powder-based activated carbon electrode; symmetric two-electrode cell	6 M KOH	172–184	1.81–1.83	1 A g^{-1}	567	[37]
Tailored dense microporous activated carbon	Dense powder-based carbon electrode; symmetric two-electrode cell	1 M $TEABF_4$	2,147	0.68	1 A g^{-1}	106	[47]
Nanocellulose/N,O co-doped graphene composite hydrogel (NGCH-150)	Binder-free graphene-based hydrogel; symmetric two-electrode cell	1 M H_2SO_4	Not report	1.35	0.3 A g^{-1}	404.6	[57]
Daikon-leaf-derived carbon monolith (VSAC)	Binder- and additive-free carbon monolith; symmetric two-electrode cell	1 M H_2SO_4	570	0.82	10 mA cm^{-2}	185	This work

The Ragone plot presented in Fig. 7 decisively highlights the kinetic trade-off between energy storage and power dissipation capabilities of the two developed solid electrodes. The VSC electrode achieves a maximum specific energy of 7.54 Wh L^{-1} at 10 mA cm^{-2}; however, this energy value significantly plummets when the system is pushed to operate at higher power density of 524 W L^{-1} at 100 mA cm^{-2}. In contrast, the VSAC electrode outperforms expectations, achieving a specific energy of up to 16.01 Wh L^{-1} while maintaining an impressive specific power of 838 W L^{-1} at

elevated current densities. This superior performance clearly demonstrates that the pore expansion through NaOH activation not only enhances the active area but also optimizes the dynamics of ion distribution within the monolithic electrode. The highly interconnected porous structure facilitates a more uniform ion adsorption and desorption process throughout the carbon volume, resulting in a gradual decrease in energy with increasing power, setting it apart from the VSC. Remarkably, the VSAC's enhanced volumetric performance is achieved even with a reduction in density due to activation. This underscores that the structural density loss is still within acceptable limits, sufficiently compensated by increased ion accessibility and improved charge transfer efficiency.

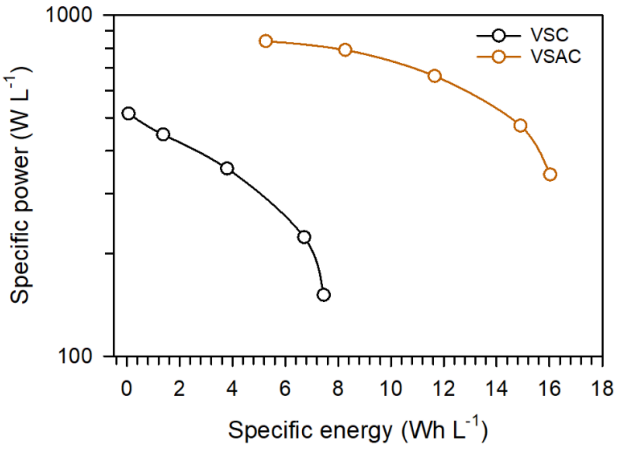

Fig. 7. Ragone plot of VSC and VSAC

4. Conclusion

Solid carbon derived from local Indonesian daikon leaves has been effectively synthesized through carbonization and physicochemical activation, resulting in a monolithic electrode that operates without adhesives and exhibits outstanding volumetric performance. This process leads to structural shrinkage and a well-developed pore network, balancing electrode density with ion accessibility. NaOH activation plays a crucial role in transforming the carbon microstructure, as confirmed by XRD, SEM, and EDS analyses. The VSAC structure demonstrates high carbon purity (95.45 wt%) and high pore development of 676 m2 g-1 compared to un-activated carbon, enhancing its electrochemical properties. Results indicate that VSAC provides a more reversible charge storage mechanism and improved ion kinetics stability than VSC. Its open pore network ensures homogeneous ion distribution, optimizing active area utilization even during rapid charging. The VSAC achieves impressive volumetric capacitance values of 169 F cm^{-3} at 1 mV s^{-1} and 185 F cm^{-3} at 10 mA cm^{-2}, with excellent capacitance retention at high current densities. Additionally, it showcases a competitive energy and power output of 16.01 Wh L^{-1} and 838 W L^{-1}, confirming the effectiveness of its design. In summary, this study demonstrates that the chemical activation strategy applied to biomass-based solid carbon maximizes surface area while balancing porosity and volumetric density. This approach paves the way for high-density biomass carbon electrodes in next-generation volumetric supercapacitor applications.

Acknowledgements

The authors sincerely thank the Directorate of Education and Community Service (DPPM) for their financial support under the *Program Penelitian Dosen Pemula* 2026 with main contract no: 260/C3/DT.05.00/PL-BARU/2026, and the derivative contract no: 219/UN19.5.1.3/AL.04/2026.

References

1. S.B. Dhavale, S.S. Patil, A.P. Patil, P.S. Patil, *Upscaling biomass derived carbon for sustainable supercapacitors: an overview,* J. Power Sources 653 (2025) 237712.
2. R. Jose, C.C. Yang, *Standardization challenges of biomass-based carbon electrodes for supercapacitors*, J. Alloys Compd. 1031 (2025) 181012.
3. G. M G, A. Sudarsanan, S. K S, B. *Saraswathyamma, A comprehensive review on advancements, challenges, and future possibilities of biomass-derived porous carbon for supercapacitors,* Prog. Solid State Chem. 82 (2026) 100572.
4. X. Zhang, J. Chen, W. Dong, J. Li, J. Zheng, H. Sun, Y. *Wang, Research progress on efficient fabrication and performance regulation of biomass-based porous carbon materials for supercapacitor electrodes: current technologies, prospects and challenges,* Biomass and Bioenergy 213 (2026) 109301.
5. A. Arjunan, S. Radhakrishnan, S.K. Kim, *Sustainable upcycling of bamboo sheath biomass to hierarchical porous carbon for next-generation supercapacitors,* Biomass and Bioenergy 212 (2026) 109305.
6. K. Wang, R. Yan, J. Liu, S. Jia, Y. Song, *Biomass-derived 2D carbon architectures: soybean pod shell conversion into N,O-heteroatoms enriched nanosheets for high performance supercapacitors,* J. Phys. Chem. Solids 216 (2026) 113686.
7. P. Meefang, T. Jorn-am, N. Thongsai, N. Meebua, *Eco-integrated electrode–electrolyte system from hemp biowaste fabricating dual N, S-doped activated carbon and pyroligneous acid electrolyte for high-performance supercapacitors,* Biomass and Bioenergy 208 (2026) 108902.
8. N.P. Reddy, R.J. Naik, N. Macherla, D.P. Joseph, R.I. Jafri, C.H. Ahn, M.R. Siddiqui, V. Gonuguntla, S.H. Park, *Biowaste-derived hierarchical activated porous carbon with heteroatom-doping (N/S) for efficient symmetrical supercapacitors: A cow urine approach,* J. Energy Storage 115 (2025).
9. N. Dhashnamoorthy, B. Nandhakumar, R. Kumar, A. V Radhamani, *Biomass to carbon nanoarchitectonics: Ultrahigh-surface area micro-mesoporous activated carbon synthesized from palmyra palm tree flowers for advanced eco-friendly supercapacitors,* Diam. Relat. Mater. 159 (2025) 112785 Contents.
10. M. Shirvani, D. Nasr Esfahani, S. B*aradari, Sustainable synthesis of hierarchical porous activated carbon from lemon tree pruning biomass for high-performance symmetric supercapacitors,* Biomass and Bioenergy 212 (2026) 109190.
11. Y. Yardım, I. Genel, C. Saka, *Integrated hydrogen generation and energy storage using pyrolysis-derived sulfur and nitrogen co-doped carbon from waste biomass,* Int. J. Hydrogen Energy 203 (2026)

153178.

12. Y. Yao, D. Ge, Y. Yu, Y. Zhang, C. Du, H. Ye, L. Wan, J. Chen, M. Xie, *Filling macro/mesoporosity of commercial activated carbon enables superior volumetric supercapacitor performances,* Microporous Mesoporous Mater. 350 (2023).
13. M.F. Hassan, M.A. Sabri, H. Fazal, A. Hafeez, N. Shezad, M. Hussain, *Recent trends in activated carbon fibers production from various precursors and applications—A comparative review,* J. Anal. Appl. Pyrolysis 145 (2020) 104715.
14. Y. Huang, H. Hsieh, Y. Chao, C. Yeh, C. Wu, *Enhancing volumetric energy and power density in supercapacitors using boron-doped holey graphene/activated carbon composites and an organic electrolyte,* J. Energy Storage 140 (2025) 118994.
15. Y. Xiao, X. Cai, W. Sun, F. Yang, *Nitrogen-enriched activated carbons via dual N-doping processes: Electrode material for high gravimetric- and volumetric-performance supercapacitor*, J. Energy Storage 56 (2022) 106040.
16. X. Zhu, J. Han, B. Wang, Y. Song, C. Shao, N. Li, H. Shi, Q. Ping, J. Zhang, M. Niu, *Wood-derived carbon electrode for all-solid-state supercapacitor with ultrahigh volumetric and area capacitances,* Ind. Crops Prod. 227 (2025).
17. M. Zhang, T. Yao, T. Xu, X. Zhou, D. Chen, L. Shen, 3*D-printed redox-active polymer electrode with high-mass loading for ultra-low temperature proton pseudocapacitor,* Adv. Powder Mater. 4 (2025) 100247.
18. H. Shi, L. Jiang, S. Sun, Z. Guo, H. Guo, S. Geng, J. Li, D. Wu, X. Zhou, L. *Sheng, Functionalized graphene microspheres for high volumetric energy density supercapacitors,* Carbon. 236 (2025) 120097.
19. Kementerian Lingkungan Hidup dan Kehutanan, Fasilitas Pengelolaan Sampah, 2025.
20. X. Geng, Z. Gong, W. Tian, M. Zhuang, H. Shang, Y. Chen, J. Li, Y. Lv, K. Bai, *Nutritional and Phytochemical Characterization of Radish Leaves : A Comprehensive Overview,* Foods 14 (2025) 3270.
21. A. Phakkhawan, A. Sakulkalavek, N. Chanlek, S. Nijpanich, *Self-activation of carbons derived from bio-waste cabbage for a green supercapacitor based on seawater electrolyte*, Sustain. Mater. Technol. 42 (2024) e01143.
22. E. Taer, N. Yanti, W.S. Mustika, A. Apriwandi, R. Taslim, A. Agustino, *Porous activated carbon monolith with nanosheet/nanofiber structure derived from the green stem of cassava for supercapacitor application*, Int. J. Energy Res. 44 (2020) 1–14.
23. R. Taslim, A. Apriwandi, E. Taer, *Novel Moringa oleifera Leaves 3D Porous Carbon-Based Electrode Material as a High-Performance EDLC Supercapacitor,* ACS Omega 7 (2022) 36489–36502.
24. T. Yu, Q. Zhou, J. Chen, W. Ma, C. Wang, S. Fan, Y. Zhang, *The synthesis of nanocellulose/B, N, F tri-doped graphene composite hydrogels for supercapacitor applications,* Vacuum 222 (2024) 113036.
25. B. Tekin, Y. Topcu, *Novel hemp biomass-derived activated carbon as cathode material for aqueous zinc-ion hybrid supercapacitors: Synthesis, characterization, and electrochemical performance,* J. Energy Storage 77 (2024) 109879.
26. G.A. Tafete, A. Uysal, N.G. Habtu, M.K. Abera, T.A. Yemata, K.S. Duba, S. Kinayyigit, *Hydrothermally synthesized nitrogen-doped hydrochar from sawdust biomass for supercapacitor electrodes,* Int. J. Electrochem. Sci. 19 (2024).
27. E. Taer, L. Pratiwi, Apriwandi, W.S. Mustika, R. Taslim, Agustino, *Three-dimensional pore structure of activated carbon monolithic derived from hierarchically bamboo stem for supercapacitor application,* Commun. Sci. Technol. 5 (2020) 22–30.
28. W. Sun, Y. Yan, Y. Wei, J. Ma, Z. Niu, G. Hu*, Catalytic Pyrolysis of Biomass: A Review of Zeolite, Carbonaceous, and Metal Oxide Catalysts,* Nanomaterials 15 (2025) 1–22.
29. K.V.G. Raghavendra, C.V.V. Muralee Gopi, V. Narayanaswamy, S. Alzahmi, B. Issa, I.M. Obaidat*, From waste to power: Advances in biomass-derived carbon materials for sustainable supercapacitor electrodes,* J. Energy Storage 156 (2026) 121558.
30. E. Taer, M. Deraman, R. Taslim, Iwantono, *Preparation of binderless activated carbon monolith from pre-carbonization rubber wood sawdust by controlling of carbonization and activation condition,* AIP Conf. Proc. 1554 (2013) 33–37.
31. J.. Gonzalez, S. Roma, J.M. Encinar, G. Martı, *Pyrolysis of various biomass residues and char utilization for the production of activated carbons*, J. Anal. Appl. Pyrolysis 85 (2009) 134–141.
32. E. Taer, A. Apriwandi, Y. Yusriwandi, W.S. Mustika, Z. Zulkifli, R. Taslim, S. Sugianto, B. Kurniasih, A. Agustino, P. Dewi, *Comparative study of CO2 and H2O activation in the synthesis of carbon electrode for supercapacitors*, AIP Conf. Proc. 1927 (2018) 030036–1–030036–6.
33. A. Sandeep, A. V. Ravindra, *Optimizing ZnCl2 activation temperature for biomass-derived porous carbons with superior energy and power density in supercapacitors*, Diam. Relat. Mater. 166 (2026) 113693.
34. A. Levent, C. Saka, *Stable electrode material for use in supercapacitor with iodine doping after sulfonation of mesoporous activated carbon particles based on microalgae biomass*, Biomass Convers. Biorefinery 15 (2025) 20803–20816.
35. J. Serafin, M. Baca, M. Biegun, E. Mijowska, R.J. Kaleńczuk, J. Sreńscek-Nazzal, B. Michalkiewicz, D*irect conversion of biomass to nanoporous activated biocarbons for high CO2 adsorption and supercapacitor applications,* Appl. Surf. Sci. 497 (2019) 143722.
36. L. Szabó, X. Xu, T. Ohsawa, K. Uto, J. Henzie, I. Ichinose, M. Ebara, *Ultrafine self-N-doped porous carbon nanofibers with hierarchical pore structure utilizing a biobased chitosan precursor,* Int. J. Biol. Macromol. 182 (2021) 445–454.
37. S. Zhang, Y. Yu, M. Xie, C. Du, J. Chen, L. Wan, Y. Zhang, *Clean production of N, O-doped activated carbon by water vapor carbonization/activation of expired coffee for high-volumetric supercapacitor,* Appl. Surf. Sci. 589 (2022) 153011.
38. E.H. Benaddi, M.R. Laamari, A. Boutouil, *Enhanced electrochemical performance and stability of biomass-derived activated carbon for supercapacitor applications*, J. Indian Chem. Soc. 102 (2025) 101927.
39. L. Gong, R. Zeng, Y. Shi, M. Yu, X. Yu, D. Sun, *Co/P co-doped bamboo-based woodceramics with a sandwich structure modified by carbon nanotube electrodeposition as supercapacitor electrodes,* Bioresour. Technol. 399 (2024) 130573.
40. M. Deraman, R. Daik, S. Soltaninejad, N.S.M. Nor, Awitdrus, R. Farma, N.F. Mamat, N.H. Basri, M.A.R. Othman*, A new empirical equation for estimating specific surface area of supercapacitor carbon electrode from X-ray diffraction,* Adv. Mater. Res. 1108 (2015) 1–7.
41. K. Kumar, R.K. Saxena, R. Kothari, D.K. Suri, N.K. Kaushik, J.N. Bohra, *Correlation between adsorption and x-ray diffraction studies on viscose rayon based activated carbon cloth,* Carbon. 35 (1997) 1842–1844. https://doi.org/10.1016/S0008-6223(97)87258-2.
42. E. Taer, E. Nur, T. Tambunan, N. Yanti, R. Taslim, *Oxygen-functionalized carbon nanofibers from kulim wood for high-performance supercapacitors via an integrated chemical–physical catalyst approach*, Commun. Sci. Technol. 10 (2025) 379–388.
43. A. Apriwandi, E. Taer, R. Farma, R.N. Setiadi, E. Amiruddin, *A facile approach of micro-mesopores structure binder-free coin/monolith solid design activated carbon for electrode supercapacitor,* J. Energy Storage 40 (2021) 102823.
44. S. Prabu, K. Chiang, *Natural bio-waste-derived 3D N/O self-doped*

heteroatom honeycomb-like porous carbon with tuned huge surface area for high-performance supercapacitor, Chemosphere In press (2024) 142400.

45. E. Taer, Sukmawati, A. Apriwandi, R. Taslim, *3D meso-macroporous carbon derived spruce leaf biomass for excellent electrochemical symmetrical supercapacitor,* Mater. Today Proc. (2023) 1–9.
46. Z. Xie, F. Kwarteng, A. Saboor, L. Dai, H. Huang, X. Yuan, Z. Luo, *Pore engineering of lignin-derived carbon for supercapacitor and batteries*, Biomass and Bioenergy 206 (2026) 108650.
47. Q. Li, Y. Jiang, Z. Jiang, J. Zhu, X. Gan, F. Qin, T. Tang, W. Luo, N. Guo, Z. Liu, L. Wang, S. Zhang, D. Jia, Z. Fan, U*ltrafast pore-tailoring of dense microporous carbon for high volumetric performance supercapacitors in organic electrolyte*, Carbon. 191 (2022) 19–27.
48. S. Sathyamoorthi, P. Chiochan, M. Sawangphruk, *High-rate aqueous/ionic liquid dual electrolyte supercapacitor using 3D graphene sponge with an ultrahigh pore volume*, Electrochim. Acta 327 (2019) 135014.
49. Y. Chen, Q. Tang, C. Shen, Y. Lei, X. Chen, *Activation-self-activation strategy for one-step preparation of Platycladus orientalis leaves based N-O-S self-doping hierarchical porous carbon for high-performance supercapacitor,* Ind. Crops Prod. 225 (2025) 120584.
50. Y. Chen, Y. Jiang, Z. Liu, L. Yang, Q. Du, K. Zhuo, *Hierarchical porous N-doped graphene aerogel with good wettability for high-performance ionic liquid-based supercapacitors,* Electrochim. Acta 366 (2021).
51. Y. Yao, Y. Yu, D. Ge, Y. Zhang, C. Du, H. Ye, L. Wan, J. Chen, M. Xie, *Nanocarbon of moderate microporosity doped with oxygenate redox pairs to achieve superior gravimetic/volumetric supercapacitor performances,* Appl. Surf. Sci. 612 (2023) 155811.
52. J. Shao, G. Zhu, L. Xie, S. Tao, Y. Zhang, J. Zhang, H. Wang, L. Zhang, C. Chen, *One-step production of N, S co-doped honeycomb-like activated carbon from instant dry yeast for high gravimetric and volumetric performance supercapacitors,* Diam. Relat. Mater. 127 (2022) 109165. https://doi.org/10.1016/j.diamond.2022.109165.
53. W. Zhang, Q. Liu, L. Guo, P. Wang, S. Liu, J. Chen, Z. Lei, *White Cabbage (Brassica oleracea L.) waste, as biowaste for the preparation of novel superabsorbent polymer gel,* J. Environ. Chem. Eng. 9 (2021).
54. T. Byambadorj, J. Zhang, Y. Li, F. Wang, Q. Liu, M. Chen, *Advanced biomass-derived carbon materials for supercapacitors: fabrication methods, structure-property relationships, modifications, and prospects,* J. Electroanal. Chem. 1000 (2026).
55. Z.M. Abdulhamid, Y. Abuhasheesh, M.E. Daoud, *Waste microalgal biomass-derived biochar electrode for sustainable high-performance supercapacitors: Experimental and computational insights,* Environ. Technol. Innov. 41 (2026) 104681.
56. Y. Liu, Q. Liu, L. Wang, X. Yang, W. Yang, J. Zheng, H. Hou, *Advanced Supercapacitors Based on Porous Hollow Carbon Nanofiber Electrodes with High Specific Capacitance and Large Energy Density,* ACS Appl. Mater. Interfaces 12 (2020) 4777–4786.
57. Y. Zhang, L. Wei, X. Liu, W. Ma, C. Lou, J. Wang, S. Fan, *Nanocellulose/N, O co-doped graphene composite hydrogels for high gravimetric and volumetric performance symmetric supercapacitors,* Int. J. Hydrogen Energy 47 (2022) 33827–33838.
58. Julnaidi, A. Amri, E. Saputra, Nofrizal, E. Taer, H*igh well-matched energy gravimetric – volumetric symmetric super-capacitor derived from hollow paper stack-like biomass-based functional carbon,* J. Chem. Technol. Biotechnol. 98 (2023) 2330–2342.
59. E. Taer, Apriwandi, H. Rusdi, A. Ismardi, R. Taslim, *Improving volumetric supercapacitors performance with additive-free solid cylinder design of O, Zn, and Cl multi-doped biomass-based carbon source,* Bioresour. Technol. Reports 24 (2023) 101631.
60. C. Zhang, Q. Fan, J. Xu, M. Huang, F. Luo, D. Wang, Z. Zheng, *Surface oxygen-containing functional groups: A key tradeoff in carbon-based energy storage devices,* Chem. Eng. J. 505 (2025) 159162.
61. K. Al, S. Başakçılardan Kabakcı, *Oxygen-rich precursors via glycerol organosolv treatment: Preparation of activated carbon from hazelnut shell and its structural components for possible use in electrodes for supercapacitors,* Int. J. Thermofluids 21 (2024) 100588.
62. E. Taer, A. Agustino, R. Farma, R. Taslim, Awitdrus, M. Paiszal, A. Ira, S.D. Yardi, Y.P. Sari, H. Yusra, S. Nurjanah, S.D. Hartati, Z. Aini, R.N. Setiadi, *The relationship of surface area to cell capacitance for monolith carbon electrode from biomass materials for supercapacitor aplication,* J. Phys. Conf. Ser. 1116 (2018) 032040.
63. D.C.T. Nguyen, S. Kim, B.S. Kim, S. Kim, S.H. Lee, *High volumetric-energy-density flexible supercapacitors based on PEDOT:PSS incorporated with carbon quantum dots hybrid electrodes,* J. Mater. Sci. Technol. 223 (2025) 1–10.
64. K. Aruchamy, S. Ramasundaram, N. Vijay, P. Jerome, S. Divya, K. Ramakrishnan, L. Fei, T.H. Oh, *Recent developments in the synthesis of heteroatom-doped and hierarchically porous carbon supercapacitor electrodes from sustainable sources,* J. Energy Storage 123 (2025).
65. E. Taer, N. Nursyafni, W. Febriani, A. Apriwandi, J.G. Manjunatha, M. Deraman, R. Taslim, *Self-single-doped hierarchical porous carbon nanofiber derived Alpinia galanga stem-based for boosted supercapacitor performance,* Mater. Lett. 360 (2024) 135954.